EDGE ARTICLE

Check for updates

Site-selective bromination of anthracene–maleimide Diels–Alder crystals for tunable afterglow and white light emission

Guangxin Yang, Tianwen Zhu, [ID] Xiang Chen, Junhao Duan, Zhipeng Zhao and Wang Zhang Yuan [ID] *

Efficient and color-tunable organic persistent room-temperature phosphorescence (p-RTP) is highly attractive for applications in colorful displays, advanced information encryption, and sensing. However, achieving such p-RTP remains challenging due to the lack of effective design strategies. Here, we introduce a synergistic chromophore-engineering approach that couples conventional and nonconventional luminophores to construct donor–acceptor adducts. These adducts exhibit dual fluorescence/p-RTP with pronounced excitation-dependent color tunability, even in crystals. Anthracene bromination (BAN/DBAN-MI) enhances SOC *via* the heavy-atom effect and increases Φ_p to 21.5% (DBAN-MI). By contrast, maleimide bromination (AN-BMI/AN-DBMI) reorganizes packing and redistributes through-space conjugation (TSC), enabling single-component white emission. Single-crystal analysis, femtosecond transient absorption spectroscopy, and theoretical calculations reveal how site-specific halogenation governs ISC and clustering-triggered emission (CTE) behaviors. This work establishes a general design principle for efficient and color-tunable organic p-RTP materials combining both aromatic and nonaromatic moieties through the CTE mechanism, highlighting their potential in multicolor displays and white-light illumination.

Introduction

Purely organic persistent room-temperature phosphorescence (p-RTP) materials have attracted growing attention owing to their long lifetimes and rich excited-state dynamics, showing great potential in data storage and encryption,[1–5] anti-counterfeiting,[6–9] sensing,[10–12] organic light-emitting diodes (OLEDs),[13–17] as well as bioimaging and diagnostics.[18–23] Achieving efficient organic p-RTP relies on two prerequisites: (i) generating sufficient triplet excitons through effective inter-system crossing (ISC) and (ii) minimizing nonradiative deactivation to favor radiative transitions.[24–27] To meet these requirements, diverse strategies have been proposed, including introducing heteroatoms, halogens, or heavy atoms to enhance spin–orbit coupling (SOC) and thus facilitate ISC,[28–30] as well as employing crystal engineering, H-aggregation, metal–organic frameworks (MOFs), and host–guest doping to suppress vibrational dissipation.[31–37] Despite notable progress, most reported afterglow materials still exhibit monochromatic emission, and achieving tunable photoluminescence (PL) and/or p-RTP within

single-component systems, especially in single crystals, remains a formidable challenge. Given the broad applicability of tunable PL materials in multicolor display, advanced encryption, and UV sensing, developing potentially extendable design strategies is of pressing significance.[38,39]

Conventional aromatic chromophores with extended π-conjugation have been extensively explored in optoelectronic materials owing to their high molar extinction coefficients (ε), precisely tunable energy levels, high color purity, and mature device compatibility.[40–42] However, their strong π–π stacking often results in self-absorption and aggregation-caused quenching (ACQ), severely diminishing PL efficiency. Moreover, such aromatic systems, composed solely of C/H/N/O elements exhibit weak SOC and insufficient orbital-type transitions to satisfy the El-Sayed rule, leading to ineffective ISC.[43–45]

In contrast, nonconventional luminophores featuring weak or non-conjugated structures display unique advantages such as aggregation-induced emission (AIE), multiple emissive centers, heteroatom- and clustering-assisted ISC, and good biocompatibility.[46–51] However, they often demonstrate weak oscillator strength, poor absorption, broad emission bands with low color purity, and sluggish charge transport, limiting their optoelectronic applications.[52–56] To address these challenges, incorporating electron-rich unconventional chromophores into small aromatic frameworks could offer an effective approach:

State Key Laboratory of Synergistic Chem-Bio Synthesis, School of Chemistry and Chemical Engineering, Frontiers Science Center for Transformative Molecules, Shanghai Key Lab of Electrical Insulation and Thermal Aging, Shanghai Jiao Tong University, No. 800 Dongchuan Rd, Minhang District, Shanghai 200240, China. E-mail: wzhyuan@sjtu.edu.cn
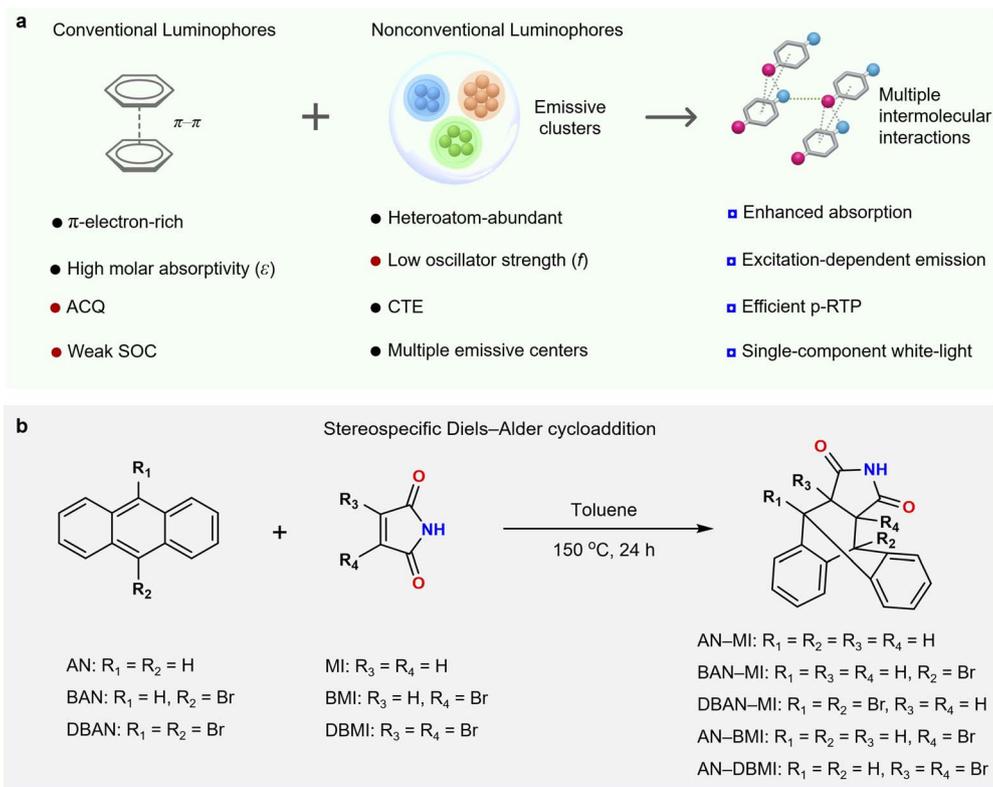
Fig. 1 (a) Schematic illustration of high-efficiency, tunable p-RTP enabled by conventional–nonconventional chromophore synergy. (b) Synthetic routes to the compounds studied herein.

the aromatic units provide strong absorption and precise energy-level control, while the nonconventional motifs introduce multiple ISC pathways—potentially enabling single-component systems that combine high efficiency, long lifetime, and tunable multicolor emission (Fig. 1a).

Herein, we introduce a conventional–nonconventional chromophore synergistic approach by embedding a maleimide unit into an anthracene scaffold *via* Diels–Alder cycloaddition (Fig. 1b and S1–S5), creating a family of stereoisomeric adducts with dual fluorescence/p-RTP. The interplay between conventional and nonconventional chromophores establishes through-space conjugation (TSC), generating multiple emissive clusters and color-tunable PL, consistent with the clustering-triggered emission (CTE) mechanism.[57,58] Abundant short-range interactions promote n–π* transitions and conformational rigidification, delivering ultralong RTP (τ_p up to 534.1 ms) and tunability. Site-selective bromination leverages the heavy-atom effect (HAE) to enhance triplet radiative pathways, raising Φ_p from 3.6% to 21.5%. Notably, the position and degree of bromination dictate molecular packing and electronic coupling, providing a powerful tool for photophysical tuning and enabling single-component white-light emission. Overall, combining conventional and nonconventional chromophores offers an effective blueprint for high-performance, color-tunable organic p-RTP and informs the design of next-generation luminescent systems.

Results and discussion

All compounds were obtained by the Diels–Alder cycloadditions between anthracene and maleimide derivatives in moderate to high yields. Their structure and purity were thoroughly characterized by spectroscopic methods and single-crystal structure determination, yielding satisfactory results. To elucidate their photophysical behaviors, AN-MI, BAN-MI, DBAN-MI, AN-BMI, and AN-DBMI crystals were systematically investigated. As shown in Fig. 2a, all five crystals display tunable PL and persistent afterglow under or after ceasing the UV excitation at 285, 312, and 365 nm, with emission color and intensity varying with excitation wavelength (λ_{ex}, Fig. S6). Taking AN-MI crystal as a representative, excitation at 312 nm affords emissions at 343, 356, 385, and 407 nm, all with nanosecond (ns) lifetimes (4.75, 6.44, 6.26, and 5.46 ns, respectively; Fig. S7a and Table S1), indicative of their fluorescence nature. In contrast, the emissions at 432 and 458 nm consist of both ns and millisecond (ms) components (Fig. S7b and Table S1, SI), the latter attributable to delayed fluorescence (DF). The delayed spectra can be continuously tuned from 505 to 585 nm, with phosphorescence lifetimes (τ_p) ranging from 125.6 to 534.1 ms (Fig. 2c and S7c), confirming the presence of multiple emissive species and strong excitation dependence.

Upon bromination of the anthracene core, triplet harvesting *via* the HAE is markedly enhanced in BAN-MI and DBAN-MI. For
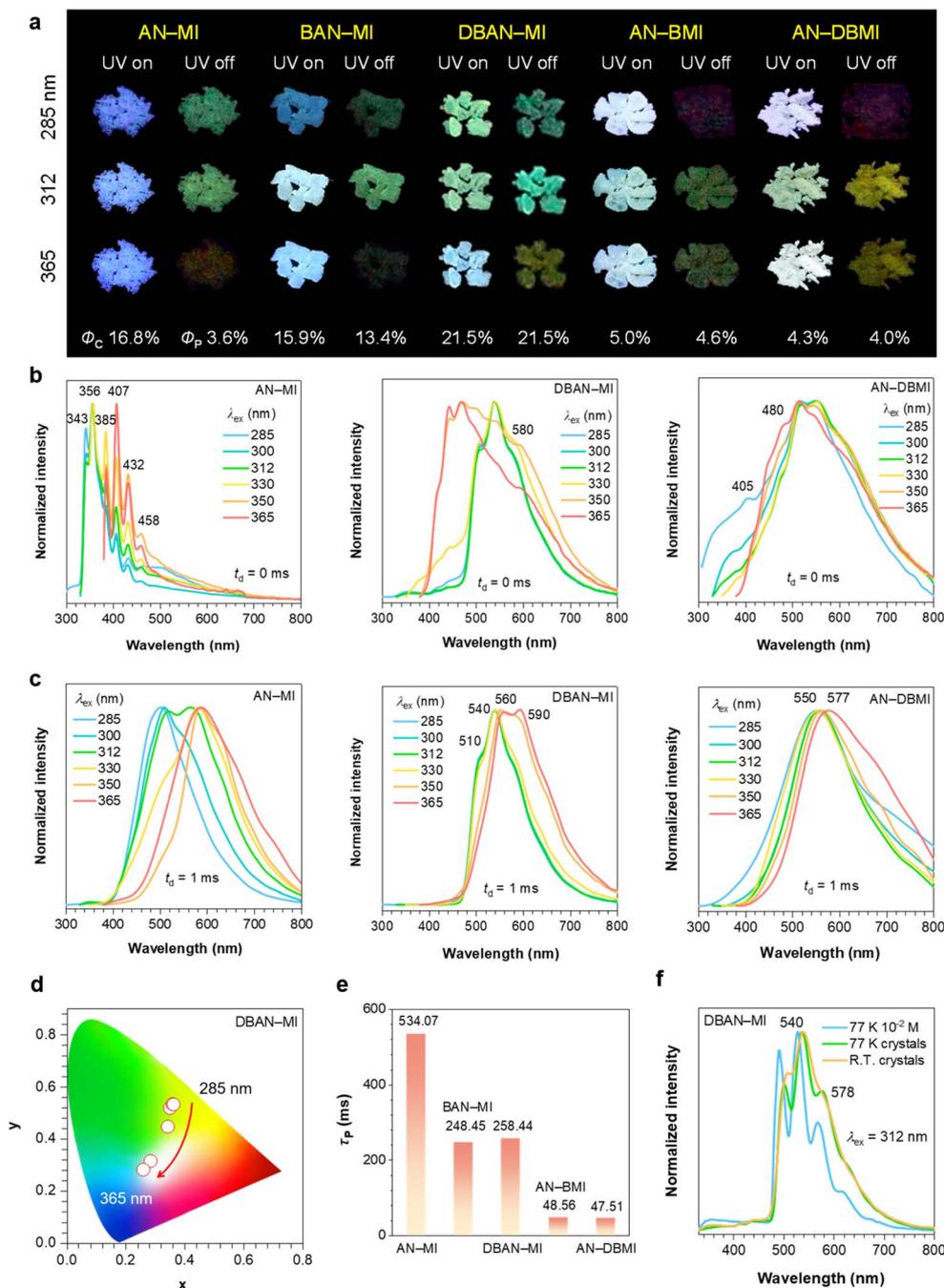
Fig. 2 (a) Photographs and total (Φ_c) and phosphorescence (Φ_p) quantum efficiency of AN-MI, BAN-MI, DBAN-MI, AN-BMI, and AN-DBMI crystals under various UV irradiations and after ceasing excitation at room temperature. (b) Prompt ($t_d = 0$ ms) and (c) delayed ($t_d = 1$ ms) emission spectra AN-MI, DBAN-MI, and AN-DBMI crystals at different λ_{ex}s; (d) CIE coordinate diagrams of prompt emission of DBAN-MI crystals at different λ_{ex}s. (e) Phosphorescence lifetime (τ_p) of all crystals. (f) Emission spectra of 10^{-2} M DBAN-MI/MTHF solution and DBAN-MI crystals at 77 K and room temperature under 312 nm excitation.

both BAN-MI (Fig. S8) and DBAN-MI (Fig. 2b and c) crystals, their prompt and delayed PL are excitation-dependent, leading to pronounced shifts in the Commission International de L'Eclairage (CIE) coordinates (Fig. 2d, S9 and S10). Lifetime analysis resolves three emission channels in BAN-MI: prompt fluorescence (ns timescale), DF (ms timescale), and phosphorescence (ms timescale) (Fig. S11 and Table S2). In contrast, with 312 nm excitation, DBAN-MI crystal exhibits nearly

overlapping prompt and delayed spectra with ms-only lifetimes, clearly demonstrating purely phosphorescent emission (Fig. S12 and Table S2). Notably, DBAN-MI crystal reaches a phosphorescence quantum efficiency (Φ_p) of 21.5%, significantly higher than AN-MI (3.6%), while BAN-MI attains 13.4% (Fig. 2a and Table S3). In comparison, AN-BMI and AN-DBMI crystals display shortened τ_p (Fig. 2e and Table S3).

Similarly, bromination on the maleimide fragment *via* Diels–Alder cycloaddition affords AN-BMI and AN-DBMI. These systems mirror the brominated-anthracene derivatives: both prompt and delayed emission exhibit marked λ_{ex}-dependence (Fig. 2b, c and S13–15). AN-BMI and AN-DBMI crystals display white to white-green PL, and upon removal of the excitation, they exhibit green and yellow afterglows, respectively. Compared to the brominated anthracene derivatives, AN-BMI and AN-DBMI crystals show a further shortened τ_p and a substantially decreased total quantum efficiency (Φ_c) (Fig. S16, S17 and Table S3). These findings indicate that bromine substitution on the maleimide unit also promotes triplet emission in the Diels–Alder adducts, albeit with increased nonradiative loss. Notably, single-component white emission can be achieved when the singlet (blue) and triplet (orange) components possess comparable intensities and are chromatically complementary.

To further elucidate the origin of the crystal emission and its aggregation-state dependence, we investigated the photophysics of DBAN-MI in 2-methyltetrahydrofuran (MTHF). As shown in Fig. S18a, the emission intensity, excited at 365 nm, increases significantly with concentration, indicating AIE feature. The prompt spectrum of the 10^{-6} M solution is nearly identical to that of the solvent, suggesting negligible intrinsic luminescence from isolated molecules. Crucially, even at 77 K, the 10^{-6} M solution remains nonemissive relative to MTHF (Fig. S18b and c). In contrast, the 10^{-2} M solution at 77 K exhibits well-resolved, vibronic-structured emission. This emission, exhibiting a slight blue shift compared to the crystal-state emission peaks, is consistent with aggregated-state emission (Fig. S18c).

To further elucidate the origin of the emission differences, we analyzed the single-crystal structures of varying compounds (Table S4). In AN-MI (Fig. 3a), intramolecular hydrogen bonding (C=O···H–C, 2.672 Å) and phenyl-imide π–π interactions (3.789 Å) rigidify the conformation. This rigidity suppresses vibrational and rotational nonradiative decay, while facilitating ISC, leading to a prolonged τ_p. In BAN-MI and DBAN-MI (Fig. 3b and S19), similar contacts are retained, augmented by heteroatom-related interactions (*e.g.*, C=O···N–H) and halogen-related short contacts (*e.g.*, C–Br···C). These additional interactions further enhance SOC, accelerate ISC, and promote triplet-exciton generation. They also favor spatially delocalized charge distribution and the formation of multiple emissive clusters. Consequently, the Φ_ps are significantly increased, although the corresponding τ_ps become shorter. The packing in AN-DBMI (Fig. 3c) differs distinctly from that of AN-MI and DBAN-MI. Although abundant heteroatom and halogen

C=O···H–C: 2.672   C=O···C–H: 3.280   C–H···H–C: 2.469   C–H···C–H: 2.791, 2.890, 2.939

N–H···Br: 3.033   O=C···C–H: 3.419   C=O···H–N: 2.343   C=O···N–H: 3.095   C=O···H–C: 2.612   C=O···Br: 3.157, 3.196
H–C···H–C: 2.686, 2.825, 2.871, 2.928

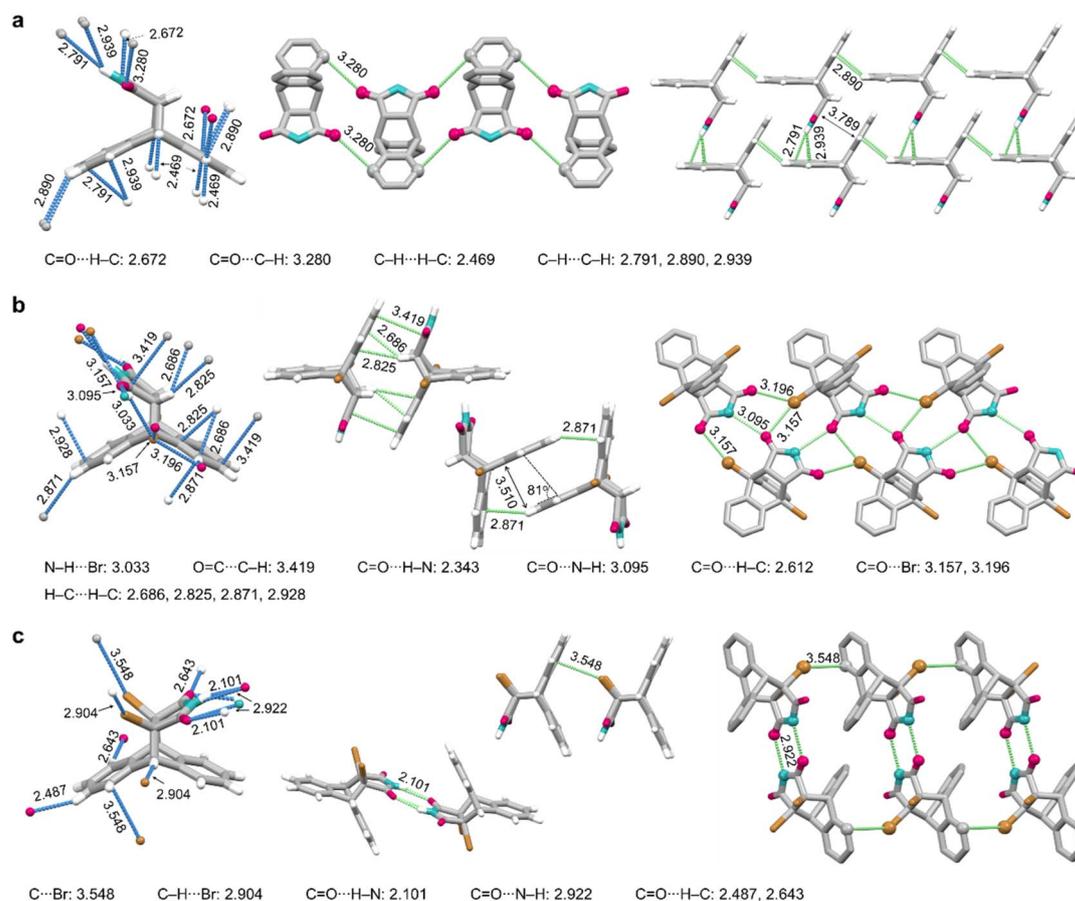C···Br: 3.548   C–H···Br: 2.904   C=O···H–N: 2.101   C=O···N–H: 2.922   C=O···H–C: 2.487, 2.643

Fig. 3 Single crystal structure and fragmental molecular packing of (a) AN-MI, (b) DBAN-MI, and (c) AN-DBMI with denoted intermolecular interactions.

contacts persist, the phenyl-imide π–π interactions are absent, which diminishes ISC efficiency. This, in turn, yields comparable singlet (blue) and triplet (orange-yellow) emission components, enabling tunable single-component white emission. Moreover, the lower hydrogen-bond density in AN-DBMI relative to DBAN-MI crystals potentially increases nonradiative pathways. Collectively, the single-crystal analyses corroborate the photophysical observations and clarify how molecular packing governs luminescent properties across this series. Notably, anthracene bromination largely preserves the primary aryl–imide packing motif, so that the packing framework is essentially conserved and the accelerated ISC can be attributed primarily to enhanced SOC *via* the heavy-atom effect. In contrast, maleimide bromination reorganizes molecular packing and TSC, reshaping the singlet–triplet balance and nonradiative loss.

To gain further insights into the emission differences among the compounds, we carried out femtosecond transient absorption (fs-TA) measurements on concentrated solutions (10^{-2} M) of AN-MI, DBAN-MI, and AN-DBMI. For AN-MI, photoexcitation immediately generates two prominent excited-state absorption (ESA) bands at ~690 and 740 nm, which reach their maxima within ~1.2 ps (Fig. 4a and d). Subsequently, both bands then decay rapidly, while a new ESA feature at ~486 nm grows in. Based on this spectral evolution, the ~690/740 nm signals are assigned to singlet-state ESA, whereas the ~486 nm band

corresponds to triplet-state ESA. Kinetic analysis of the ~740 nm trace reveals two processes: τ_1, attributed to ultrafast relaxation within the singlet manifold, and τ_2, assignable to ISC from S_1 to T_n. From τ_2, a k_{ISC} of ~1.3×10^9 s^{-1} for AN-MI was estimated (Fig. 4g and S20). For DBAN-MI, two ESA bands emerge promptly at ~436 and 545 nm (Fig. 4b and e). The latter feature decays rapidly, while the former rises and reaches its maximum at ~278 ps. Subsequently, the ~436 nm signal decays only very slowly within the observed window. Kinetic decomposition yields an ISC component τ_2 corresponding to a k_{ISC} of ~8.0×10^9 s^{-1}, indicating a substantially accelerated ISC upon bromination on anthracene (Fig. 4h and S21). In contrast, AN-DBMI displays a distinct kinetic signature. Following 312 nm excitation (Fig. 4c and f), a clear ESA at ~368 nm appears immediately and peaks at ~9.4 ps, then decays as a new ESA at ~420 nm slowly rises. The 368 and 420 nm bands are assignable to singlet- and triplet-state ESA, respectively. Fitting the 368 nm kinetics yields an ISC lifetime of 1906 ps, corresponding to a k_{ISC} of 5.25×10^8 s^{-1} (Fig. 4i and S22). Thus, AN-DBMI undergoes significantly slower ISC than AN-MI and DBAN-MI, underscoring the site-specific effect of bromination on SOC and ISC efficiency. These fs-TA results align well with the steady-state photophysics: AN-MI, with its moderate ISC, exhibits a long τ_p and moderate Φ_p; DBAN-MI, with faster ISC, shows a higher Φ_p and a shorter τ_p; and AN-DBMI, with the slowest ISC, displays reduced Φ_p and shortened τ_p. Nonetheless, the
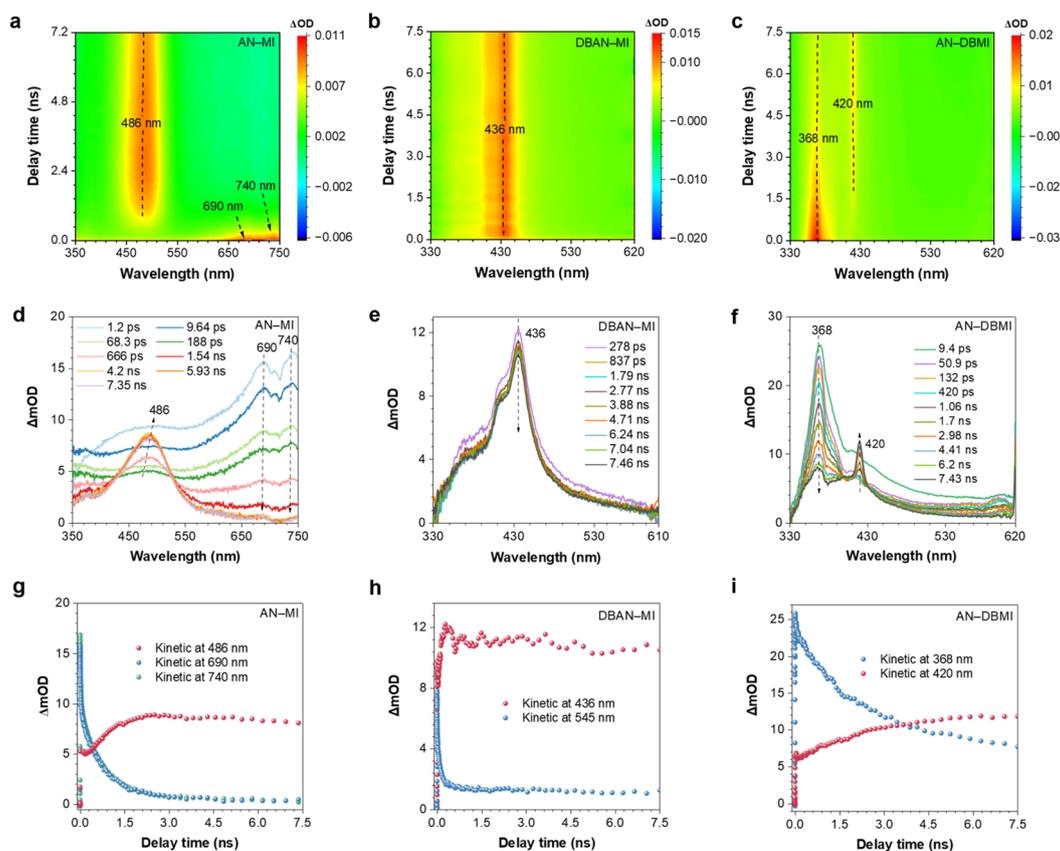

Fig. 4 TA results of 10^{-2} M AN-MI/ACN, DBAN-MI/ACN, and AN-DBMI/ACN solutions: (a–c) time-resolved TA contour plots; (d–f) TA spectra at different delay times; (g–i) kinetic traces at selected wavelengths.

comparable singlet (blue) and triplet (orange-yellow) contributions make single-component white emission more accessible.

To gain theoretical insights, time-dependent density functional theory (TD-DFT) calculations were performed on the monomers and dimers of varying compounds. These calculations yielded the corresponding electron distribution and singlet/triplet energy levels. For AN-MI (Fig. 5a and S22), the monomer displays electron delocalization within and between the phenyl and imide rings. In its dimer (Dimer-1) a clear aryl–imide through-space electronic coupling emerges at LUMO+1. Upon bromination of the aromatic ring, the overall electron density increases. In BAN-MI (Dimer-1) at the LUMO level and in DBAN-MI (Dimer-2) at LUMO+1/+2/+3, stronger aryl–imide interactions are evident. These enhanced interactions are indicative of effective TSC that facilitates ISC and promotes triplet emission (Fig. 5b, S23 and S24). Strikingly, bromination on the maleimide unit reorganizes the electron distribution and

the extent of TSC. In AN-DBMI dimers, the aryl–imide interaction weakens, while imide–imide delocalization is reinforced. This modification reduces ISC rates, consistent with the fs-TA observations (Fig. 5c and S25). In addition, the S_1 and T_1 energies progressively decrease from AN-MI to DBAN-MI and then to AN-DBMI (Fig. 5d and Tables S5–S8), paralleling the red-shifted afterglow observed across the series.

Taken together, these results delineate a coherent emission mechanism for this family of Diels–Alder adducts (Fig. 5e). In AN-MI, intra- and intermolecular aryl–imide interactions produce multiple emissive clusters, rigidify the conformation, and promote ISC, giving rise to long-lived (534.1 ms) and tunable phosphorescence. Bromination on the aryl ring in BAN-MI and DBAN-MI largely preserves the overall packing arrangement and aryl–imide contacts. Furthermore, the HAE further enhances ISC, boosting Φ_p and shortening τ_p. In contrast, bromination on the maleimide ring (AN-BMI, AN-
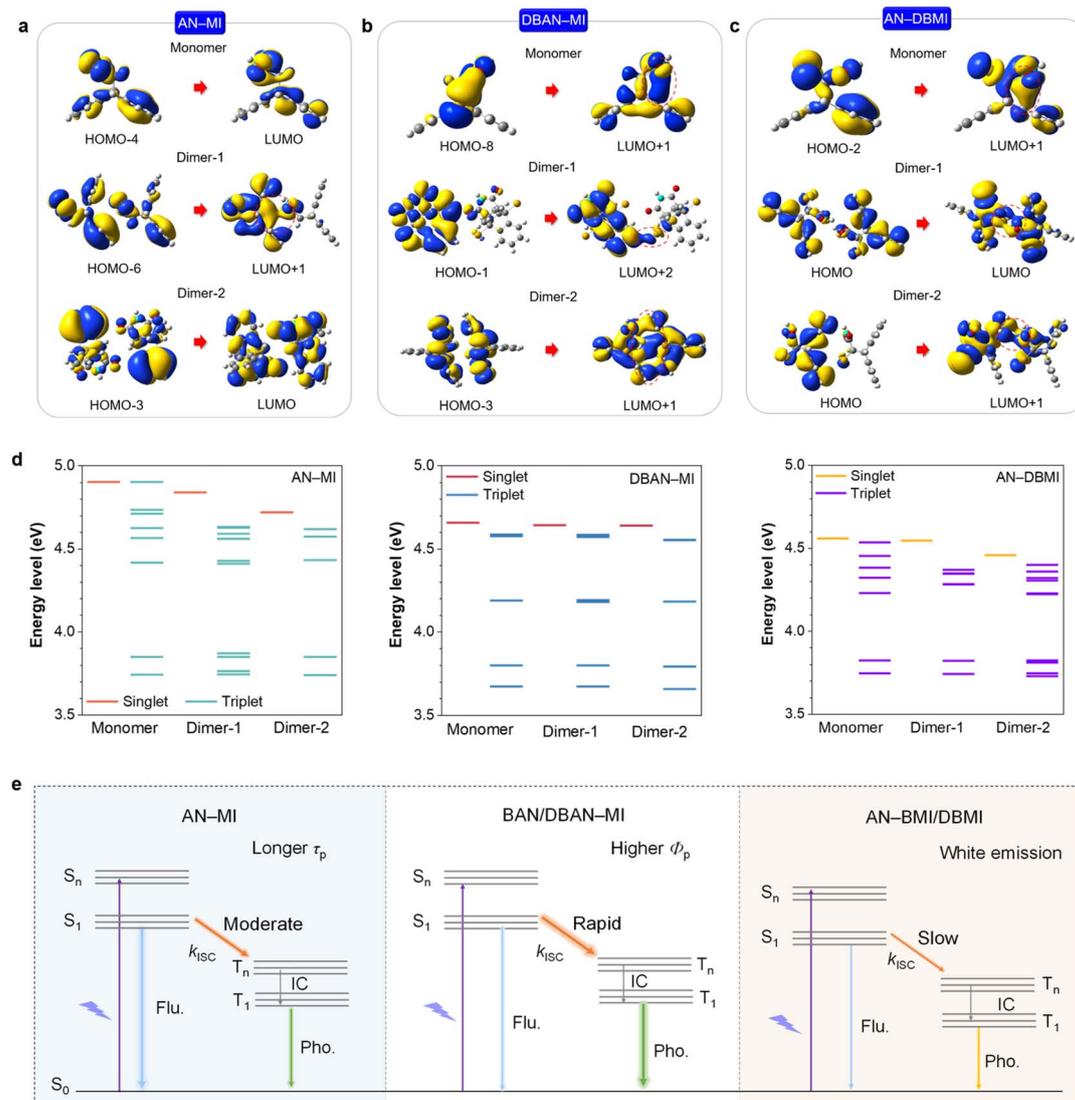

Fig. 5 HOMO, LUMO, and other related energy levels electron densities of the selected monomers and dimers of (a) AN-MI, (b) DBAN-MI, and (c) AN-DBMI. (d) Excitation energy diagrams of monomer and dimers of AN-MI, DBAN-MI, and AN-DBMI. (e) Schematic of the photophysical processes in AN-MI, BAN/DBAN-MI, and AN-BMI/DBMI.
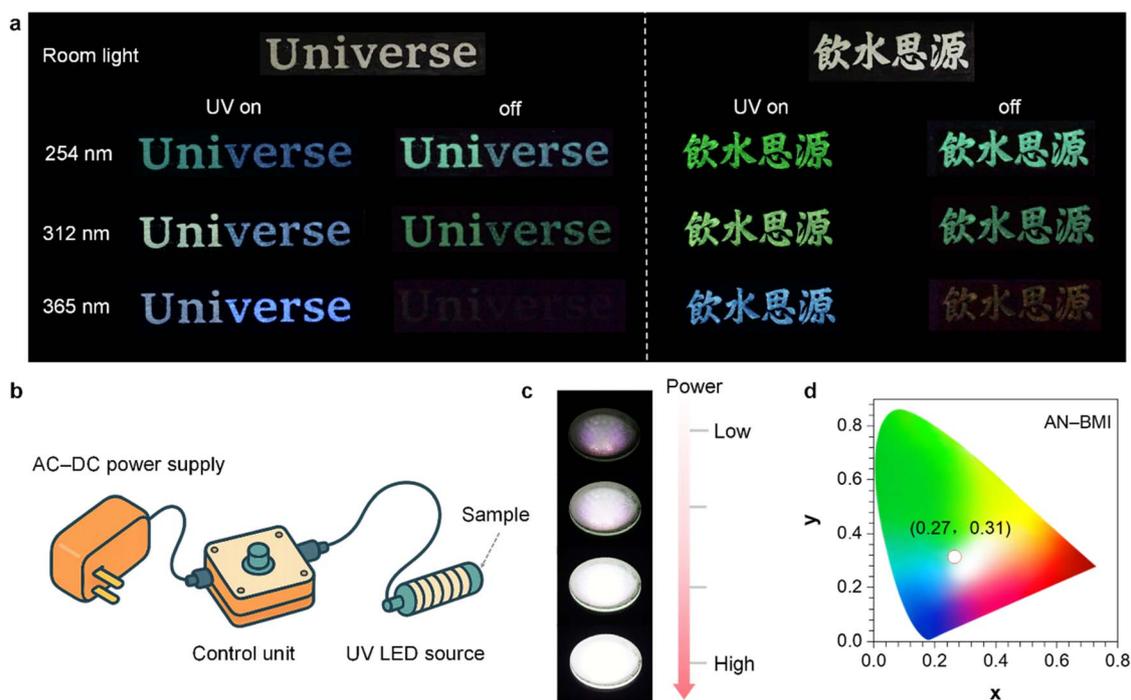
Fig. 6 (a) Patterns spelling Universe and the Chinese idiom '飲水思源', where 'Uni' is filled with BAN-MI, 'verse' with AN–DBMI, and the idiom with DBAN-MI. Photographs under UV excitation at different wavelengths and after removal of UV light. (b) Schematic diagram of a white-light illumination device. (c) Photographs of white-light emission at different excitation powers. (d) CIE coordinate diagram corresponding to the sample's emission.

DBMI) triggers a significant reorganization of molecular packing, with imide–imide interactions becoming dominant. This altered packing reduces conformational rigidity and slows ISC, consequently lowering Φ_c and τ_p. However, the introduction of halogen bonding/contacts diversifies the clustered emissive species and broadens tunability. Crucially, the balanced singlet and triplet emissions facilitate single-component white-light emission.

Leveraging the synergy between conventional and nonconventional chromophores enables efficient, photo-stimuli-responsive afterglow systems that support programmable, multi-scenario demonstrations. Fig. 6a illustrates multicolor display and information encryption. In the word 'Universe', the 'Uni' region is filled with BAN-MI powder, whereas 'verse' is filled with AN-DBMI. The idiom '飲水思源' is patterned with DBAN-MI powder. These patterns show distinct PL colors and afterglow durations under different UV excitations and in the light-off state. By switching emissive components and excitation wavelength, time-gated readout enables multichannel encryption. In sum, dual control by λ_{ex} and molecular structure allows for the scalable fabrication of multicolor afterglow objects that unite aesthetics with function. It is also noted that the single-component white emission of the brominated derivatives empowers their potential for white-light illumination. As shown in Fig. 6b, a thin film of AN-BMI was thermally evaporated onto a transparent quartz wafer and mounted in the device. By tuning the excitation power, the white-light intensity can be continuously tuned in intensity (Fig. 6c), whose CIE coordinates are (0.27, 0.31), closely approximating ideal white-light (Fig. 6d).

Conclusions

In summary, we present a versatile blueprint for color-tunable p-RTP in Diels–Alder crystals by combining conventional and nonconventional chromophores. The anthracene–maleimide Diels–Alder adducts show dual fluorescence/p-RTP emission with excitation-dependent color tunability. Site-selective bromination provides two distinct outcomes. Anthracene bromination enhances SOC *via* the heavy-atom effect and increases Φ_p to 21.5% in DBAN-MI crystals. Maleimide bromination reorganizes packing and shifts intermolecular coupling toward imide–imide contacts, which balances blue fluorescence and orange phosphorescence to afford single-component white emission. More broadly, synergistically combining conventional and nonconventional chromophores with site-selective heavy-atom engineering offers an effective route to purely organic, color-tunable p-RTP materials for diverse optoelectronic applications.

Author contributions

W. Z. Y. conceived the initial project. T. Z. and W. Z. Y. designed the experiments. G. Y. and T. Z. conducted the synthesis, spectroscopic characterization, and single-crystal analysis. G. Y. performed the ultrafast spectroscopy. G. Y., X. C., and J. D.

carried out the theoretical calculations and analysed the results. T. Z. supported G. Y. in drafting the manuscript. W. Z. Y. supervised the project and revised the manuscript. All authors have given approval to the final version of the manuscript.

Conflicts of interest

There are no conflicts to declare.

Data availability

CCDC 2523773–2523776 ((AN-MI), (BAN-MI), (DBAN-MI) and (AN-DBMI)) contain the supplementary crystallographic data for this paper.[59a–d]

The data supporting this study are available within the article and the supplementary information (SI). Any additional data are available from the corresponding authors upon reasonable request. Supplementary information: detailed experimental procedures, characterization data and photophysical data. See DOI: https://doi.org/10.1039/d6sc00542j.

Acknowledgements

References

1 L. Gao, J. Huang, L. Qu, X. Chen, Y. Zhu, C. Li, Q. Tian, Y. Zhao and C. Yang, *Nat. Commun.*, 2023, **14**, 7252.

2 X. Yao, J. Wang, D. Jiao, Z. Huang, O. Mhirsi, F. Lossada, L. Chen, B. Haehnle, A. J. C. Kuehne, X. Ma, H. Tian and A. Walther, *Adv. Mater.*, 2021, **33**, 2005973.

3 L. Ding and X.-d. Wang, *J. Am. Chem. Soc.*, 2020, **142**, 13558.

4 Y. Tian, J. Yang, Z. Liu, M. Gao, X. Li, W. Che, M. Fang and Z. Li, *Angew. Chem., Int. Ed.*, 2021, **60**, 20259.

5 S. Cai, X. Yao, H. Ma, H. Shi and Z. An, *Aggregate*, 2023, **4**, e320.

6 X. Yu, H. Zhang and J. Yu, *Aggregate*, 2021, **2**, 20.

7 D. Wang, J. Gong, Y. Xiong, H. Wu, Z. Zhao, D. Wang and B. Z. Tang, *Adv. Funct. Mater.*, 2023, **33**, 2208895.

8 J. Zhang, Z. Wang, X. Huo, X. Meng, Y. Wang, H. Suo and P. Li, *Laser Photonics Rev.*, 2024, **18**, 2300751.

9 Y. Lei, W. Dai, J. Guan, S. Guo, F. Ren, Y. Zhou, J. Shi, B. Tong, Z. Cai, J. Zheng and Y. Dong, *Angew. Chem., Int. Ed.*, 2020, **59**, 16054.

10 M. S. Kwon, D. Lee, S. Seo, J. Jung and J. Kim, *Angew. Chem., Int. Ed.*, 2014, **53**, 11177.

11 Y. Zhou, W. Qin, C. Du, H. Gao, F. Zhu and G. Liang, *Angew. Chem., Int. Ed.*, 2019, **58**, 12102.

12 S. K. Mellerup and S. Wang, *Chem. Soc. Rev.*, 2019, **48**, 3537.

13 B. S. B. Karunathilaka, U. Balijapalli, C. A. M. Senevirathne, S. Yoshida, Y. Esaki, K. Goushi, T. Matsushima,

A. S. D. Sandanayaka and C. Adachi, *Nat. Commun.*, 2020, **11**, 4926.

14 T. Wang, X. Su, X. Zhang, X. Nie, L. Huang, X. Zhang, X. Sun, Y. Luo and G. Zhang, *Adv. Mater.*, 2019, **31**, 1904273.

15 L. X. Hou, H. Ju, X. P. Hao, H. Zhang, L. Zhang, Z. He, J. Wang, Q. Zheng and Z. L. Wu, *Adv. Mater.*, 2023, **35**, 2300244.

16 J. Han, D. Ma, L. Jiang, Y. Zhang, M. Dong, Y. Deng, Y. Geng, R. Huang, C. Xu, X. Zheng, G. Dong and L. Duan, *Adv. Mater.*, 2025, e14723.

17 Z. Yu, Y. Wu, L. Xiao, J. Chen, Q. Liao, J. Yao and H. Fu, *J. Am. Chem. Soc.*, 2017, **139**, 6376.

18 F. Xiao, H. Gao, Y. Lei, W. Dai, M. Liu, X. Zheng, Z. Cai, X. Huang, H. Wu and D. Ding, *Nat. Commun.*, 2022, **13**, 186.

19 Y. Wang, H. Gao, J. Yang, M. Fang, D. Ding, B. Z. Tang and Z. Li, *Adv. Mater.*, 2021, **33**, 2007811.

20 F. Lin, H. Wang, Y. Cao, R. Yu, G. Liang, H. Huang, Y. Mu, Z. Yang and Z. Chi, *Adv. Mater.*, 2022, **34**, 2108333.

21 X. Zhen, Y. Tao, Z. An, P. Chen, C. Xu, R. Chen, W. Huang and K. Pu, *Adv. Mater.*, 2017, **29**, 1606665.

22 S. M. A. Fateminia, Z. Mao, S. Xu, Z. Yang, Z. Chi and B. Liu, *Angew. Chem., Int. Ed.*, 2017, **56**, 12160.

23 G. Yang, S. Hao, Y. Dan, L. Dang, H. Zhang, Q. Zhang, A. Li, M.-D. Li and W. Z. Yuan, *Adv. Mater.*, 2025, **37**, 2418042.

24 X. Yan, H. Peng, Y. Xiang, J. Wang, L. Yu, Y. Tao, H. Li, W. Huang and R. Chen, *Small*, 2022, **18**, 2104073.

25 W. Zhao, Z. He and B. Z. Tang, *Nat. Rev. Mater.*, 2020, **5**, 869.

26 T. Zhang, X. Ma, H. Wu, L. Zhu, Y. Zhao and H. Tian, *Angew. Chem., Int. Ed.*, 2020, **59**, 11206.

27 N. Gan, H. Shi, Z. An and W. Huang, *Adv. Funct. Mater.*, 2018, **28**, 1802657.

28 Z. He, W. Zhao, J. W. Y. Lam, Q. Peng, H. Ma, G. Liang, Z. Shuai and B. Z. Tang, *Nat. Commun.*, 2017, **8**, 416.

29 T. Zhu, T. Yang, Q. Zhang and W. Z. Yuan, *Nat. Commun.*, 2022, **13**, 2658.

30 Z. Yang, Z. Mao, X. Zhang, D. Ou, Y. Mu, Y. Zhang, C. Zhao, S. Liu, Z. Chi, J. Xu, Y.-C. Wu, P.-Y. Lu, A. Lien and M. R. Bryce, *Angew. Chem., Int. Ed.*, 2016, **55**, 2181.

31 O. Bolton, K. Lee, H.-J. Kim, K. Y. Lin and J. Kim, *Nat. Chem.*, 2011, **3**, 205.

32 E. Hamzehpoor and D. F. Perepichka, *Angew. Chem., Int. Ed.*, 2020, **59**, 9977.

33 R. Gao, M. S. Kodaimati and D. Yan, *Chem. Soc. Rev.*, 2021, **50**, 5564.

34 G. Yang, S. Hao, Z. Zhang, W. Z. Yuan, M.-D. Li and L. Dang, *Nat. Commun.*, 2025, **16**, 8927.

35 Z. Wang, C.-Y. Zhu, Z.-W. Wei, Y.-N. Fan and M. Pan, *Chem. Mater.*, 2020, **32**, 841.

36 Z. An, C. Zheng, Y. Tao, R. Chen, H. Shi, T. Chen, Z. Wang, H. Li, R. Deng, X. Liu and W. Huang, *Nat. Mater.*, 2015, **14**, 685.

37 G. Yang, S. Hao, X. Deng, X. Song, B. Sun, W. J. Hyun, M.-D. Li and L. Dang, *Nat. Commun.*, 2024, **15**, 4674.

38 D. Liu, B. Kan, X. Ke, N. Zheng, Z. Xie, D. Lu and Y. Liu, *Adv. Energy Mater.*, 2018, **8**, 1801618.

39 J. Zhu, Z. Ke, Q. Zhang, J. Wang, S. Dai, Y. Wu, Y. Xu, Y. Lin, W. Ma, W. You and X. Zhan, *Adv. Mater.*, 2018, **30**, 1704713.

40 G.-J. Shi, K.-K. Tan, S.-Y. Liu, H. Zhang, H.-R. Hu, K.-P. Wang, L.-Z. Xu, M. Li and Z.-Q. Hu, *Chem. Commun.*, 2022, **58**, 13596.

41 Q. Miao and K. Pu, *Adv. Mater.*, 2018, **30**, 1801778.

42 M. Einzinger, T. Wu, J. F. Kompalla, H. L. Smith, C. F. Perkinson, L. Nienhaus, S. Wieghold, D. N. Congreve, A. Kahn, M. G. Bawendi and M. A. Baldo, *Nature*, 2019, **571**, 90.

43 J. Guo, Y. Zhen, H. Dong and W. Hu, *J. Mater. Chem. C*, 2021, **9**, 16843.

44 X. Chen, X. Zhang, X. Xiao, Z. Wang and J. Zhao, *Angew. Chem., Int. Ed.*, 2023, **62**, e202216010.

45 Y. Huang, J. Xing, Q. Gong, L.-C. Chen, G. Liu, C. Yao, Z. Wang, H.-L. Zhang, Z. Chen and Q. Zhang, *Nat. Commun.*, 2019, **10**, 169.

46 Z. Zhao, A. Li and W. Z. Yuan, *Acc. Chem. Res.*, 2025, **58**, 612.

47 S. Tang, T. Yang, Z. Zhao, T. Zhu, Q. Zhang, W. Hou and W. Z. Yuan, *Chem. Soc. Rev.*, 2021, **50**, 12616.

48 D. A. Tomalia, B. Klajnert-Maculewicz, K. A. M. Johnson, H. F. Brinkman, A. Janaszewska and D. M. Hedstrand, *Prog. Polym. Sci.*, 2019, **90**, 35.

49 N. Jiang, C.-Y. Zhu, K.-X. Li, Y.-H. Xu and M. R. Bryce, *Macromolecules*, 2024, **57**, 5561.

50 Q. Li, Y. Tang, W. Hu and Z. Li, *Small*, 2018, **14**, 1801560.

51 C. X. Chen, H. W. Cai, X. L. Sun, W. M. Wan and B. Q. Huang, *ChemPlusChem*, 2025, **90**, e202400633.

52 A. Li, Z. Zhao, G. Yang, Q. Zhang, X. Chen and W. Z. Yuan, *Chem. Sci.*, 2025, **16**, 11530.

53 S. Tang, Z. Zhao, J. Chen, T. Yang, Y. Wang, X. Chen, M. Lv and W. Z. Yuan, *Angew. Chem., Int. Ed.*, 2022, **61**, e202117368.

54 D. Pinotsi, L. Grisanti, P. Mahou, R. Gebauer, C. F. Kaminski, A. Hassanali and G. S. Kaminski Schierle, *J. Am. Chem. Soc.*, 2016, **138**, 3046.

55 H. Li, J. Gu, Z. Wang, J. Wang, F. He, P. Li, Y. Tao, H. Li, G. Xie, W. Huang, C. Zheng and R. Chen, *Nat. Commun.*, 2022, **13**, 429.

56 R. B. Restani, P. I. Morgado, M. P. Ribeiro, I. J. Correia, A. Aguiar-Ricardo and V. D. B. Bonifácio, *Angew. Chem., Int. Ed.*, 2012, **51**, 5162.

57 Q. Zhou, B. Cao, C. Zhu, S. Xu, Y. Gong, W. Z. Yuan and Y. Zhang, *Small*, 2016, **12**, 6586.

58 Y. Gong, Y. Tan, J. Mei, Y. Zhang, W. Yuan, Y. Zhang, J. Sun and B. Z. Tang, *Sci. China: Chem.*, 2013, **56**, 1178.

59 (*a*) CCDC 2523773: Experimental Crystal Structure Determination, 2026, DOI: 10.5517/ccdc.csd.cc2qq61q; (*b*) CCDC 2523774: Experimental Crystal Structure Determination, 2026, DOI: 10.5517/ccdc.csd.cc2qq62r; (*c*) CCDC 2523775: Experimental Crystal Structure Determination, 2026, DOI: 10.5517/ccdc.csd.cc2qq63s; (*d*) CCDC 2523776: Experimental Crystal Structure Determination, 2026, DOI: 10.5517/ccdc.csd.cc2qq64t.